Optical Materials 128 (2022) 112433

Contents lists available at ScienceDirect

Optical Materials

journal homepage: www.elsevier.com/locate/optmat

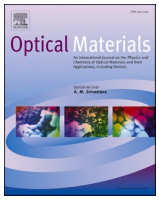

Research Article

Temperature quenching of Cr^{3+} in $ASc(Si_{1-x}Ge_x)_2O_6$ (A=Li/Na) solid solutions

Arnoldus J. van Bunningen [a,*], Atul D. Sontakke [a], Sadakazu Wakui [b], Andries Meijerink [a]

[a] Debye Institute, Utrecht University, Utrecht, 3508 TA, Netherlands
[b] NICHIA Corperation, Tokushima, 777-0132, Japan

A B S T R A C T

Blue absorbing near infrared (NIR) emitting phosphors are a promising class of materials for phosphor converted NIR LEDs, which can be used in compact NIR spectrometers. Preferably, these phosphors have a broad emission spectrum and show negligible luminescence quenching at LED operating temperatures (100 °C). Here, we investigated $ASc(Si_{1-x}Ge_x)_2O_6$ (A = Li/Na, x = 0,0.2,0.4,0.6,0.8,1) solid solutions doped with Cr^{3+} to tune and optimize the emission maximum and bandwidth to cover the full 700–1100 nm range. With increasing Ge content an emission redshift was observed, along with emission band broadening at intermediate Ge/Si ratio, which is explained by disorder around Cr^{3+} in the second coordination sphere (mixed Si/Ge). Temperature dependent emission spectra and luminescence decay curves were measured between 90 K and 670 K to determine the quenching temperature T_Q. With increasing Ge content T_Q drops from 550 K to below 400 K. Interestingly, Cr^{3+} emission in the highly symmetric site in $LiScSi_2O_6$ shows a strongly temperature dependent lifetime before thermal quenching sets in. DFT calculations on $LiScSi_2O_6$ indicate that asymmetric vibrations at the Sc site are involved and calculated phonon energies were confirmed by measuring FTIR. Our study indicates that a solid solution is a promising way to increase the emission bandwidth. However, with increasing Ge content T_Q decreases. An optimum Ge-content in $LiSc(Si_{1-x}Ge_x)_2O_6:Cr^{3+}$ is x = 0.2–0.4 as it redshifts the NIR band maximum close to 900 nm and offers a FWHM bandwidth around 180 nm, while keeping the thermal quenching temperature high enough for application in NIR-LEDs.

1. Introduction

The discovery of the efficient blue (In,Ga)N-based LED has revolutionized the lighting industry. In the development of better phosphor converted white light LEDs an important focus is on narrow band red and green phosphors to enhance the colour quality and overall efficiency of the LEDs. Beyond this traditional quest for more efficient lighting with better colour rendering, new fields are emerging. An upcoming field is human centric lighting aimed at spectral shaping of the LED output to realize health benefits, for example through phosphors with a cyan emission colour to influence the circadian rhythm. Control over the spectral distribution of LED lighting is also important in horticulture as plant growth can be optimized by the lamp spectrum, also including emission wavelengths outside the visible range as plants respond to wavelengths in the near infrared (NIR) [1]. Another upcoming application in NIR LEDs concerns chemical sensing. Vibrational overtones of organic molecules are in 700–1500 nm spectral window and NIR absorption spectroscopy can be used to monitor the presence and concentrations of (bio-)molecules [2,3]. Broadband NIR sources can be used for spectral scanning to observe and analyse these absorption lines. This results in a non-destructive and facile chemical analysis method. This technique has great potential in applications such as healthcare, agriculture, or food.

Traditionally incandescent lamps are used in NIR spectrometers. However, their short life-span (<2000 h), large size and low efficiency make them unattractive. Recent developments are focussed on phosphor-converted NIR LEDs (pc-LEDs) based on spectral conversion of blue LED light to NIR emission by broadband NIR emitters. The pc-LED broadband emitters provide a compact and efficient broadband NIR source for bio-chemical sensing. Miniaturization using NIR pc-LEDs combined with compact CCD-type spectrometers will allow for cheap sensing functionalities that can be incorporated in portable devices and mobile phones. The performance of the NIR pc-LED strongly depends on the NIR phosphor and presently Cr^{3+} is the most widely explored activator for broadband NIR emitting phosphors owing to its ability to provide broadband NIR emission with excellent efficiency.

The desired properties of phosphors for NIR pc-LEDs include an emission wavelength between 700 and 1000 nm (or longer wavelengths if combined with detectors other than crystalline silicon), broad bandwidth, preferably close to 200 nm, strong absorption in the blue and limited thermal quenching of the emission up to at least ~100 °C [4]. Cr^{3+} ticks most of these boxes as it can have a broadband $^4T_2 \rightarrow {}^4A_2$

* Corresponding author.
E-mail address: a.j.vanbunningen@uu.nl (A.J. van Bunningen).

https://doi.org/10.1016/j.optmat.2022.112433
Received 23 March 2022; Received in revised form 26 April 2022; Accepted 29 April 2022
Available online 13 May 2022

emission, typically centred between 750 and 900 nm and bandwidths between 100 and 150 nm, depending on the local environment and has broad band d-d absorption in the cyan or blue making it suitable for pc-LEDs. A problem is however thermal quenching of the $^4T_2 \rightarrow {}^4A_2$ emission that often sets in well below 100 °C. From the Tanabe-Sugano diagram for the 3 d^3 configuration it is clear that a small crystal field splitting is required to have the $^4T_2$ level as the lowest excited state (giving broad band emission) and not the ^2E level which gives a sharp line emission around 700 nm.

A few years ago, Osram light AG was the first to introduce pc-LED product that shows broadband NIR emission based on Cr^{3+} NIR phosphor(s). This device has an efficiency of 7–8% [4], which leaves room for improvement. Many studies have appeared since and show that thermal quenching is an issue for Cr^{3+} NIR phosphors. The local ligand coordination is important but also the second coordination sphere affects the Cr $^{3+}$ luminescence quenching temperature. For example, research by Małysa et al. [5] on Sc garnets has shown that the local environment in the first and second coordination sphere is crucial to the quenching temperature. Broad band $^4T_2 \rightarrow {}^4A_2$ emission is essential but even for Cr^{3+} in several hosts not showing the ^2E line emission, the crystal field is still too large resulting in a $^4T_2$ emission band that is at higher in energy (towards 750 nm) than desired [5–8]. Other hosts have a more desirable emission towards 900 nm [9] but suffer from temperature quenching of the luminescence. Unfortunately, there is trend for Cr^{3+} emission to show lower thermal quenching temperatures upon red shifting the emission and upon band broadening, as can be understood from the configurational coordinate diagram (larger offset between ground state and excited state and lower excited state energy lead to a lower quenching temperature T_Q). This opposite relation between the desired thermal quenching temperature on the one hand and the emission maximum and bandwidth on the other, make it challenging to find a phosphor that meets all requirements. Amongst several hosts explored for Cr^{3+} broadband NIR emission, recently the clinopyroxenes $LiScSi_2O_6$ and $NaScSi_2O_6$ have shown good thermal stability up until 100–150 °C while still the emission maximum is at wavelengths above 850 nm [10,11]. Pyroxenes are a group of minerals with the formula XYSi2O6 where X and Y are different metal ions. The structures consist of layers of silicate chains sandwiched between layers of metal cations.

In this research we focus on the $(Li,Na)Sc(Si_{1-x}Ge_x)_2O_6$: Cr^{3+} system. By varying the Si and Ge, the influence of the second coordination sphere on the emission of Cr^{3+} can be studied. The peak position as well as the FWHM of the Cr^{3+} emission is studied as function of the Ge concentration with the goal to optimize emission wavelength and FWHM. By introducing disorder, inhomogeneous broadening can increase the emission band without affecting the offset in the configurational coordinate diagram. We study the effect of the solid solutions on the thermal quenching of the luminescence. Two series of phosphors are investigated: $LiSc(Si_{1-x}Ge_x)_2O_6$, $NaSc(Si_{1-x}Ge_x)_2O_6$ both doped with 1% Cr. A relatively low Cr^{3+} concentration is used to avoid Cr–Cr interactions at neighbouring Sc sites. Our composition and temperature dependent measurements show that substituting part of the Si by Ge is beneficial for the FWHM (broader) and emission maximum (redshift) but lowers the luminescence quenching temperature, making the optimum composition a trade-off between the different performance parameters.

2. Materials and methods

For the synthesis of the samples Li_2CO_3 (MERCK, >99%), $NaCO_3$(-Sigma Aldrich, >99,95), $Sc_2(C_2O_4)_3$ $5H_2O$. (Scandium oxalate, precipitated from dissolved Sc-metal), SiO_2 (Amorphous Silica Pore Size 6 nm, Sigma Aldrich, >99,9%), GeO_2 (highways International, 6 N), Cr_2O_3 (Merck, 99,9%) was used. Two series were made for $LiSc(Si_{1-x}Ge_x)_2O_6$: 1% Cr^{3+} and $NaSc(Si_{1-x}Ge_x)_2O_6$: 1% Cr^{3+} (with x = 0,0.2,0.4,0.6,0.8,1). It is assumed that the Cr^{3+} substitutes on the Sc^{3+} position. The precursors were mixed for about 15 min in stoichiometric amounts using an agate pestle and mortar with sufficient acetone to wet the powder. For the $LiSc(Si_{1-x}Ge_x)_2O_6$ samples 10 mol% extra Li_2CO_3 was added as a flux. The synthesis was done by heating the precursors to 1100 °C under air atmosphere and annealed for 8 h. Nano porous silica was necessary to maximize the contact surface of the micro grains. Scandium oxalate was used to increase the reactivity of Sc^{3+} ions and accelerate the synthesis.

The powders were examined using powder X-ray diffraction for its phase purity. A Phillips PW1729 X-ray generator, Cu source was used at 40 kV operating voltage and 20 mA current. The step size resolution was 0.02° 2θ. The photoluminescence (PL) spectroscopy was performed by using an Edinburgh Instruments FLS-920 fluorescence spectrometer. The PL and PL excitation (PLE) spectra were recorded using a 450 W Xe lamp as excitation source and a Hamamatsu H5509 photomultiplier tube (PMT) detector. PL decay measurements were performed by using a tuneable optical paramagnetic oscillator (OPO) Opotek Opolette HE 355II pulsed laser (pulse width: 10 ns; repetition rate: 20 Hz) as excitation source, and the emission was recorded by a Hamamatsu R928 PMT detector. For temperature dependent studies a temperature-controlled stage from Linkam Scientific (THMS600) was used for measurements in a −190 °C–450 °C temperature range.

For the FTIR absorption measurements the samples were pressed into KBr pellets by mixing 1 mg of sample with 200 mg of dry KBr. FTIR measurements were performed with a Bruker Vertex 70. Spectra were recorded from 400 cm^{-1} - 4000 cm^{-1}, with a KBr beam splitter, a DLaTGS D301 detector, and a mid IR source.

First-principles total energy calculations [12] were performed based on density functional theory (DFT) [13,14] using the Projector Augmented Wave (PAW) as implemented in Vienna ab-initio simulation package [15,16]. Frozen core approximation was combined with PAW and the valence electron configurations are $1s^22s^1$ for Li, $3s^23p^63d^14s^2$ for Sc, $3s^23p^2$ for Si, $2s^22p^4$ for O. Exchange and correlation were treated with the generalized gradient approximation [17]. The wave functions were expanded in a plane-wave basis set with kinetic energy cut off of 600eV. 6 × 6 × 6 Monkhorst-pack *k*-points mesh were used for the integration in *k* space in the Brillouin zone for the primitive unit cell. The structural optimization were performed until each component of the interatomic force became less than 1.0 × 10^{-3}eV/Å. Phonon energy calculations were carried out using the density functional perturbation theory [18,19] and PHONOPY software [20]. A supercell of 2 × 2 × 2 and 2 × 2 × 2 Monkhorst-pack *k*-points mesh were used for phonon energy calculations.

3. Results

The as-synthesized samples were visually inspected and exhibit a clear trend in sample body colour as a function of composition. For both series of samples, phosphors with a high Ge concentration are pink while the Si rich sample are light green in colour (supporting information, Fig. S1). This change of colour represents the differences in crystal field and covalency as Si is substituted with bigger Ge ions in the lattice. This causes a shift of the Cr absorption bands to lower energies. The body colour is used in the figures to identify the composition of samples by varying the colour from pink (Ge) to green (Si) and colour shades between pink and green for results obtained for the (Si,Ge) solid solutions.

3.1. XRD

$LiScSi_2O_6$ (LSS), $LiScGe_2O_6$(LSG), $NaScSi_2O_6$(NSS) $NaScGe_2O_6$(NSG) are all isostructural. When looking at the XRD patterns in Fig. 1 one notices that for both the LSS/LSG and the NSS/NSG series the peaks shift to lower 2θ angles with increasing Ge concentration, for example the (3 1 0) peak shifts from 31° to 30° in LSS/LSG and from 30.5°-29.5° in the NSS/NSG series. The shift to lower 2θ with increasing Ge is expected as a result of lattice expansion for increasing Ge content (with a larger 0.39 Å ionic radius for Ge^{4+} vs. 0.26 Å for Si^{4+} [21]). The continuous shift indicates that a solid solution is formed with Si and Ge mixed

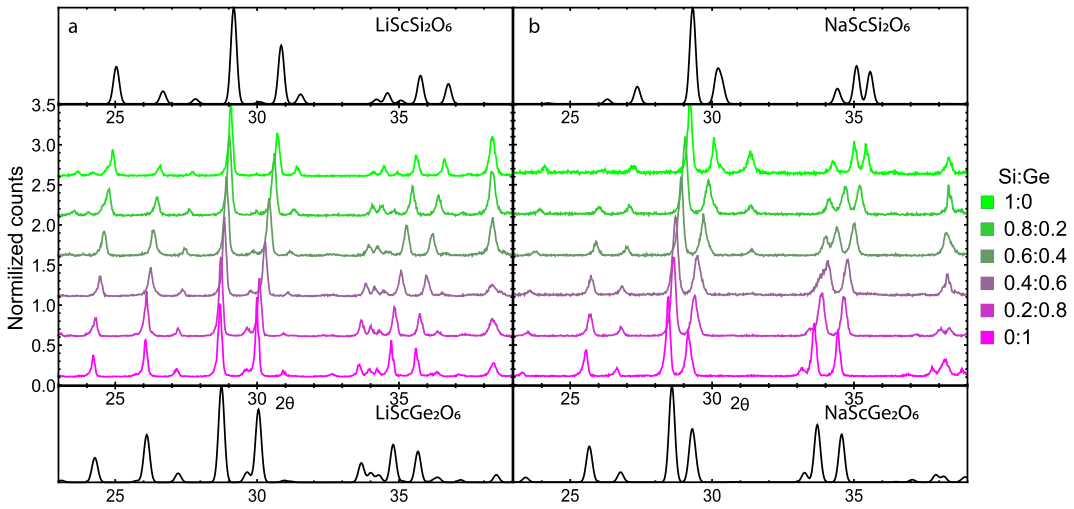

Fig. 1. X-ray powder diffraction patterns of: **(a)** $LiSc(Si_{1-x}Ge_x)_2O_6$:1%$Cr^{3+}$with the reference of $LiScSi_2O_6$(LSS) [45] and $LiScGe_2O_6$ (LSG) [46]shown above and below. **(b)** $NaSc(Si_{1-x}Ge_x)_2O_6$:1%$Cr^{3+}$with the reference of $NaScSi_2O_6$(NSS) [32] and $NaScGe_2O_6$ (NSG) [33]shown above and below.

homogeneously throughout the matrix. Some weak extra peaks for the $LiScSi_2O_6$ sample can be seen around $2\theta = 24°$. We attribute this to $Li_2Si_2O_5$. Full XRD patterns are available in the supporting information (Fig. S2.).

The crystal structure is composed of alternating layers of tetrahedrally coordinated Si^{4+}/Ge^{4+} and layers with octahedral Sc^{3+} and polyhedral Na^+ or Li^+, as can be seen in Fig. 2. The Sc ions have two Sc nearest neighbours giving rise to one dimensional strings through the crystal. On either side of the string there are Na or Li atoms. These Na or Li atoms together with tetravalent cations atoms create a cylindrical channel though the crystal. The cylindrical structure may enhance ion diffusion and would explain the relative low temperature (1100 °C) needed for the synthesis where most silicates require temperatures above 1200 °C.

3.2. Photoluminescence

To investigate the role of the host composition on the luminescence properties, emission spectra of Cr^{3+} in LSS, LSG, NSS and NSG were recorded and are shown in Fig. 3. The NIR emission has a peak maximum around 860 nm in the silicates and it redshifts to 900 nm for Cr^{3+} in the germanates. For the photoluminescence excitation (PLE) spectra three clear bands are observed, one just above 300 nm and around 480 nm and 700 nm. These observations are in agreement with earlier results for the luminescence of Cr^{3+} in $NaScSi_2O_6$ and $LiScSi_2O_6$ [10,11,22]. The 700 nm band shows some interesting features with some dips around the band maximum. Comparing the intensity of the 480 and the 700 nm peak we observe that the 480 nm peak is relatively stronger than the 700 nm peak for the germanate samples. The luminescence spectra can be understood using the d^3 Tanabe Sugano diagram. The broadband emission is the $^4T_2 \rightarrow {}^4A_2$ emission. The bands at 320, 480 and 700 nm in the PLE spectra can be assigned to the transition from the $^4A_2$ ground state to the $^4T_1(^4P)$, $^4T_1(^4F)$ and $^4T_2$ (^4F) excited states. The small dips in the $^4A_2 \rightarrow {}^4T_2$ excitation band around 700 nm are explained by Fano anti-resonance due to mixing of the $^4T_2$ state with resonant $^2T_1$ and ^2E states [23,24].

In Fig. 4 the luminescence spectra of Si–Ge solid solutions are shown. Both for the LSS/LSG series as well as the NSS/NSG series the band maxima redshift with increasing Ge content, as is also plotted in Fig. 4d. The full width at half maximum (FWHM) of the emission bands for both series initially increase with Ge content, level off and then decrease again for the pure Ge sample (Fig. 4c). The redshift of the emission peak with an increase in Ge is explained by a weaker crystal field upon substituting Si with the larger Ge which lowers the energy difference between the $^4T_2$ and $^4A_2$ states. The weaker crystal field cannot simply be explained by a change in Cr–O distance. Based on the XRD data the average O–Sc distances *d* have been calculated: NSS 2.102 Å (±0.068), NSG 2.106 Å (±0.065), LSS 2.107 Å (±0.084) and LSG 2.109 Å (±0.078). The slight increase in Sc–O (and thus Cr–O) distance upon substituting Si by Ge cannot explain the redshift through the Cr – Ligand distance dependence of the CF splitting Δ_O. The very small difference in *d* and the theoretical d^5 dependence of Δ_O would only cause a redshift less than 1%. Clearly, covalency effects play a role as will be discussed below. The variation FWHM of the Cr^{3+} emission bands for the solid solutions are explained by an increase of disorder in the second coordination sphere where a mixed Si/Ge coordination is varies for different Cr^{3+} ions and causes variations in the emission band maximum (shifting to longer wavelengths for a Ge-rich coordination). This gives rise to inhomogeneous broadening and the sum of all the emission spectra is observed in the spectrum as a broadened band. The largest FWHM is realized for $LiSc(Si_{1-x}Ge_x)_2O_6$:1%Cr^{3+} with x = 0.4–0.8. The FWHM of 0.28 eV corresponds to ~180 nm FWHM around 880 nm which is much

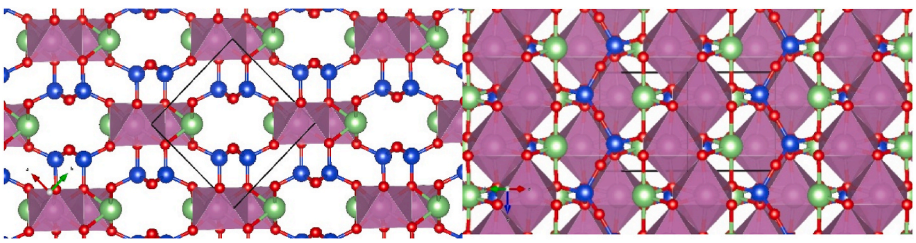

Fig. 2. Crystal structure of $LiScsi_2O_6$ perpendicular to the c axis. Green: Li, Blue: Si, Red: O Purple: Sc. One can observe layers of tetrahedral silicate groups alternating with layers of Li and Sc. In b a perpendicular projection of a is shown. Here we can clearly see the strings of interconnected octahedral Sc ions separated by Li atoms.

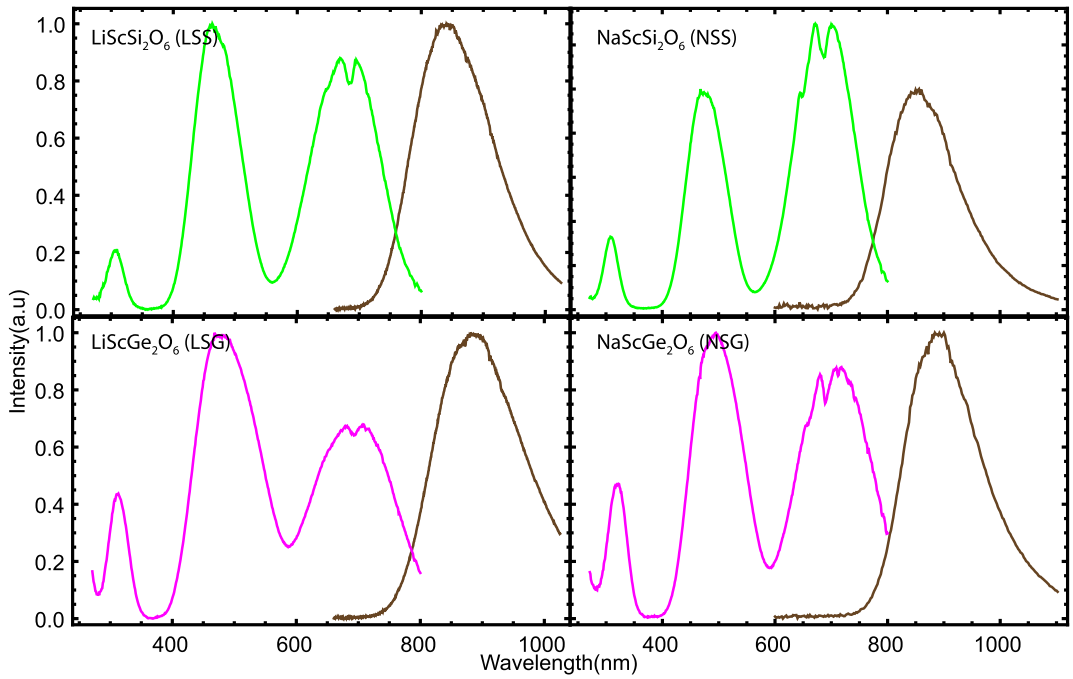

Fig. 3. PL and PLE spectra of LSS, NSS, LSG, NSG doped with 1% Cr^{3+} measured at room temperature. The PL curves are shown in brown and are excited at 480 nm. The PLE curves, green or pink, are measured for 900 nm emission.

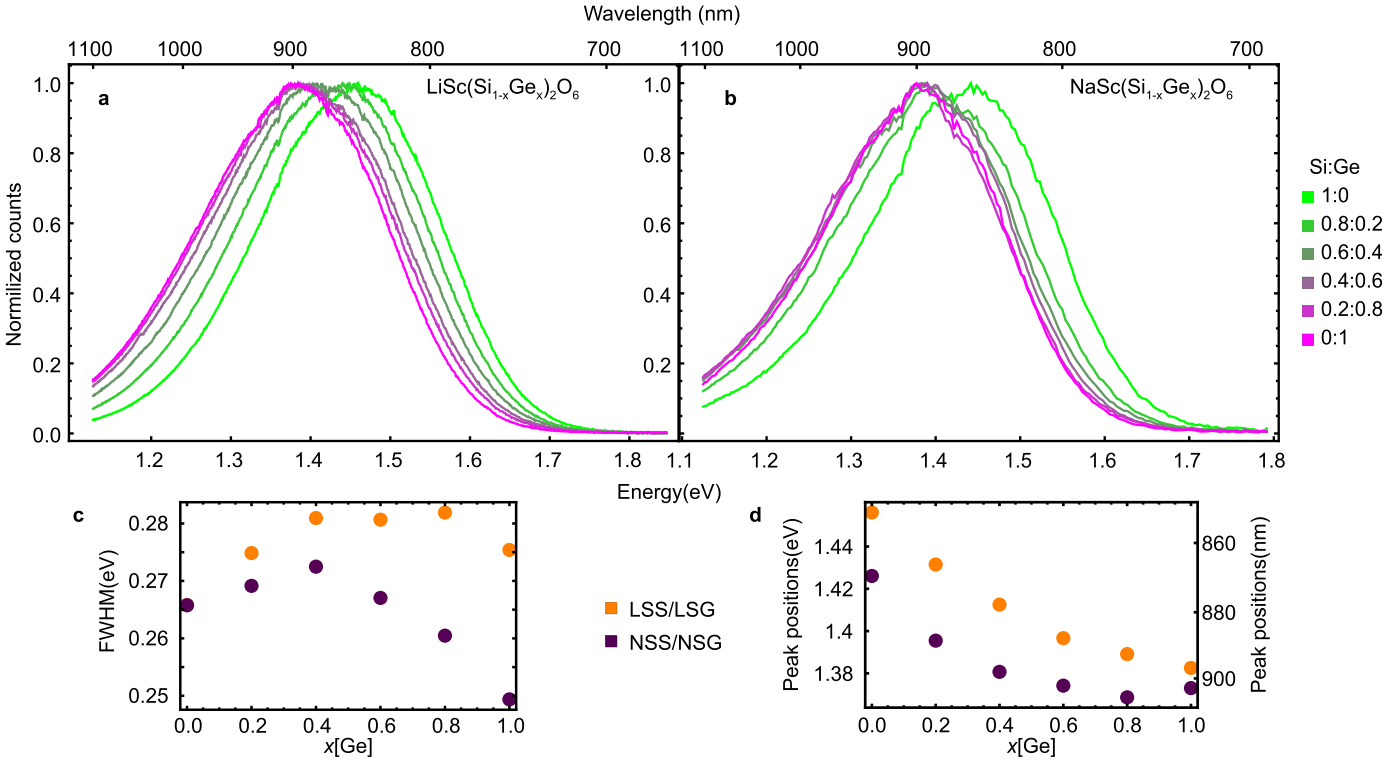

Fig. 4. PL spectra of **(a)** $LiSc(Si_{1-x}Ge_x)_2O_6$:1%Cr^{3+} and **(b)** $NaSc(Si_{1-x}Ge_x)_2O_6$:1%Cr^{3+} solid solutions. All the spectra were obtained by exciting at 480 nm at room temperature. **(c)** The full width half max (FWHM) of both the series as a function of Ge content **(d)** emission peak positions as determined by fitting to a Gaussian.

larger than for other Cr^{3+} based NIR phosphors where typical values for the FWHM of the $^4T_2$-$^4A_2$ emission band range from 100 to 150 nm [6, 24–26].

To determine the PL peak maxima, the spectra were converted to an energy scale [27], after which a Gaussian fit was done using the data points between 1.55 and 1.31eV (800 and 950 nm) as shown in Fig. 4a and b. This helps to determine peak positions even though it is important to realize that the theoretical peak shape is not Gaussian. The peak maximum shows a clear dependence on Ge content. For Cr^{3+} in LSS the emission is at slightly shorter wavelength (850 nm) then for NSS (870 nm) but with increasing Ge content the peak positions redshift to almost the same wavelength (900 nm). A shift in $^4T_2 \rightarrow {}^4A_2$ emission is often

related to the Sc–O distance [5,28] The difference in band maximum between LSS and NSS cannot be explained by only a variation in distance as the change in Sc–O is ~0.5%: 2.102 to 2.107 Å for LSS and NSS respectively. Also, here changes in covalency contribute to the redshift in NSS.

To further investigate the role of cation substitution on the optical properties of Cr^{3+}, the PLE spectra, as shown in Fig. 5, were analysed to determine the crystal field and Racah parameters. After converting the spectra to an energy scale [27] the peak positions of the $^4A_2$ to $^4T_1(^4F)$ and $^4T_2$ excitation bands were determined by fitting to a Gaussian. From these peak positions, the crystal field parameter Dq (note $\Delta_O = 10$ Dq) and Racah parameter B were found using the Tanabe-Sugano diagrams [29]]. The results are shown in Table 1. Some interesting trends can be observed for the pure compounds and solid solutions. With increasing Ge content, the crystal field splitting decreases. For the $NaSc(Si_{1-x}Ge_x)_2O_6$ series Dq drops from 1,443 cm^{-1} to 1398 cm^{-1} and for $LiSc(Si_{1-x}Ge_x)_2O_6$ from 1469 to 1436 cm^{-1}. The Racah parameter B also lowers as a function of Ge content, from 670 cm^{-1} to 610 cm^{-1} for $NaSc(Si_{1-x}Ge_x)_2O_6$ and from 665 cm^{-1} to 608 cm^{-1} for $LiSc(Si_{1-x}Ge_x)_2O_6$. Increasing Ge content increases the covalent bonding character, and this decreases the crystal field strength and gives a stronger nephelauxetic effect (smaller B). These effects are in line what is observed by B Małysa in and $Sr_{1-x}Ca_xSc_2O_4:Cr^{3+}$. With increasing concentration of the smaller cation Ca^{2+} cation the Dq value increased. Similarly in $CaAl_{12}O_{19}/SrAl_{12}O_{19}$, $YAl_3(BO_3)_4/GdAl_3(BO3)_4$, $YSc_3(BO_3)_4/GdSc_3(BO_3)_4$ the Dq is the highest for the smaller ion and the B parameter is larger [28,30,31]. For example, in $Sr_{1-x}Ca_xSc_2O_4:Cr^{3+}$ the crystal field splitting Dq increases with Ca-content while B increases. In $Sr_{1-x}Ca_xSc_2O_4$ a significant decrease in Sc–O distance explains the increase in Dq for higher Ca^{2+} content, which at the same time makes the bonding more ionic, explaining the increase in B. Note that, as discussed above, changes in the average Sc–O distance $NaSc(Si_{1-x}Ge_x)_2O_6$ and $LiSc(Si_{1-x}Ge_x)_2O_6$ are less than 1 pm and are too small to explain the shift in excitation and emission bands [32,33].

Finally, it is interesting to observe that the ratio between the $^4T_1$ to $^4T_2$ peaks changes with Ge concentration. The ratio of $^4T_2$: $^4T_1(^4F)$ for LSS/LSG goes from 0.9 to 0.7 and for the NSS/NSG system from 1.3 to 0.9. The relative intensity of the $^4T_1(^4P)$ increases along with that of the $^4T_1(^4F)$ band. This change in $^4T_1$ to $^4T_2$ ratio is often observed but has not received much attention [5,28]. A very strong change was reported by Back et al. for Cr^{3+} in two polymorphs of Ga_2O_3, a high symmetry alpha phase and a lower symmetry beta phase [34]The PLE showed a tremendous difference in the $^4T_1$: $^4T_2$ excitation intensity ratio (1:3 for alpha, 2:1 for beta) [34] and was explained by the influence of admixture of ^2E and $^2T_1$ states in the overlapping (resonant) $^4T_2$ states. Whether this explanation is correct or not requires further research.

Table 1
Crystal field parameters (10 Dq) and Racah parameter (B) as obtained from the PLE spectra for the 12 different samples of $NaSc(Si_{1-x}Ge_x)_2O_6$ and $LiSc(Si_{1-x}Ge_x)_2O_6$ at room temperature.

Sample	$^4A_2$->$^4T_2$(cm^{-1})	$^4A_2$->$^4T_1$(cm^{-1})	10Dq/B	B (cm^{-1})	Dq (cm^{-1})
NSS	14,440	20,840	21.7	665	1443
x = 0.2	14,300	20,560	22.1	648	1432
x = 0.4	14,240	20,390	22.5	633	1424
x = 0.6	14,160	20,210	22.8	620	1414
x = 0.8	14,080	20,060	23	611	1405
NSG	13,990	19,950	23	608	1398
LSS	14,650	21,200	21.8	674	1469
x = 0.2	14,590	20,920	22.8	643	1466
x = 0.4	14,530	20,760	23.2	629	1459
x = 0.6	14,450	20,590	23.5	618	1452
x = 0.8	14,370	20,440	23.4	609	1425
LSG	14,290	20,260	24.1	596	1436

Symmetry does seem to play a role. To quantify the deviation from perfect octahedral symmetry the angles between the oxygen atoms around the scandium position were analysed. The six O atoms will have fifteen interatomic distances and directions (twelve nearest neighbours and three opposing distances). The angles between all the vectors (105 in total) were compared to the angles a perfect octahedron would have and the average angle deviation for each compound was calculated to be for LSS 2.201°, LSG 2.775°, NSS 2.777°, NSG 3.360°. We can see that the deviation from perfect octahedral symmetry becomes stronger from LSS to LSG and from NSS to NSG and is accompanied by an increase in relative intensity of both $^4T_1$ bands. Similar results were seen $Ca_{1-x}Sr_xSc_2O_4$. With increasing Sr content, the $^4A_2 \rightarrow {}^4T_1$ increases. The $SrSc_2O_4$ has more distorted Sc sites with respect to $CaSc_2O_4$ [28]. An opposite trend is observed in $Bi_2Al_{4-x}Ga_xO_9:Cr^{3+}$ but here also the bandgap (smaller for the gallate) and ionic radius of the cation site for Cr^{3+} (larger in the gallate) changes which will affect the breaking of the parity selection rule [35] The analysis presented suggests that breaking the parity selection rules by deviations from inversion symmetry is more pronounced for the $^4A_2 \rightarrow {}^4T_1$ than for the $^4A_2 \rightarrow {}^4T_2$ transition but further research to fully understand the strong variations of the $^4A_2 \rightarrow {}^4T_1$ to $^4A_2 \rightarrow {}^4T_2$ absorption strengths is needed.

In Fig. 6 luminescence decay curves are shown for the $^4T_2$ emission in the various samples. Emission decay dynamics are insightful to obtain radiative decay rates which are, especially for symmetry forbidden transitions, dependent on the coordination symmetry. Typically, luminescence decay can be described with a single exponential function. In solid solutions the local environment can differ between luminescing ions, and this gives rise to deviations from single exponential decay. A

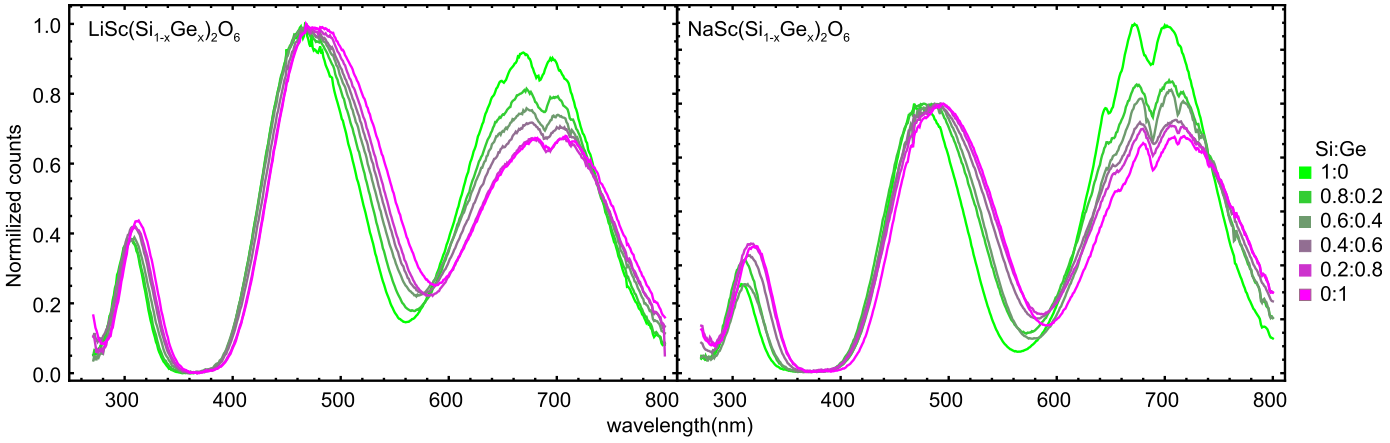

Fig. 5. PLE spectra of $LiSc(Si_{1-x}Ge_x)_2O_6:1\%Cr^{3+}$ and $NaSc(Si_{1-x}Ge_x)_2O_6:1\%Cr^{3+}$ solid solutions. All the spectra were obtained by monitoring emission at 900 nm at room temperature.

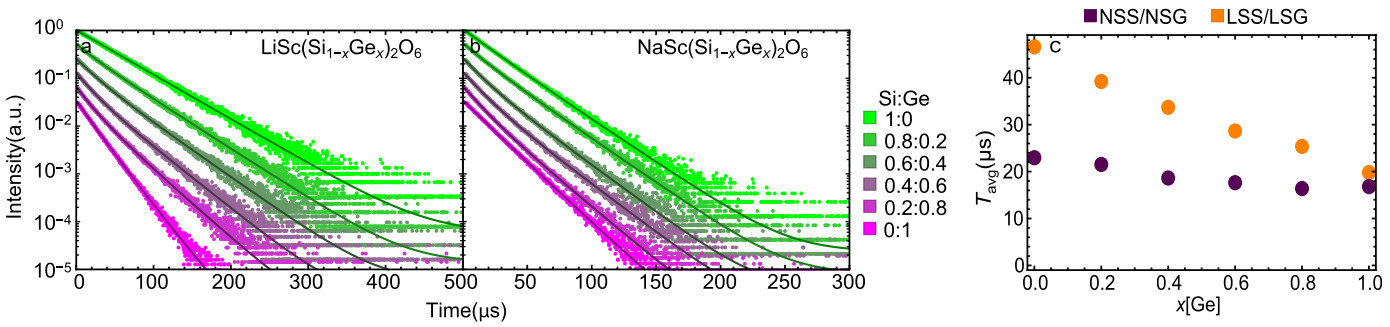

Fig. 6. Decay curves at room temperature of **(a)** $LiSc(Si_{1-x}Ge_x)_2O_6$:1%Cr^{3+} solid solutions and **(b)** $NaSc(Si_{1-x}Ge_x)_2O_6$:1%Cr^{3+} solid solutions. Excited at 480 nm and monitored at 800 nm. The solid lines show the fits.

bi-exponential fit provides a good approximation and therefore the emission decay curves for Cr^{3+} in the solid (Si,Ge) solutions was fitted to:

$$I(t) = A_1 e^{-t/\tau_1} + A_2 e^{-t/\tau_2} + C \quad (1)$$

Here *I(t)* is the intensity as a function of time, A_1 and A_2 are pre-exponential factors and τ_1 and τ_2 represent the emission lifetimes of differently coordinated Cr^{3+} ions and *C* takes background noise into account. The average lifetime can be calculated using:

$$\tau_{avg} = \frac{A_1\tau_1^2 + A_2\tau_2^2}{A_1\tau_1 + A_2\tau_2} \quad (2)$$

In Fig. 6c luminescence lifetime for the Cr^{3+} emission is plotted as function of composition. The lifetimes are longer in the Li-based samples. With increasing Ge content, the lifetime decreases, and this effect is stronger for the Li series. The longest emission lifetime observed for the highest symmetry coordination (LSS), as expected. The decrease in lifetime with Ge content is consistent with lowering of the symmetry and an increase in the covalent character which lowers the energy of opposite parity states favouring admixture to break the parity selection rule.

Based on the optical characterization of the two series of samples, it is evident that for application in a NIR-LED the $LiSc(Si_{1-x}Ge_x)_2O_6$ samples with a Ge content around 50% are the most promising based on the largest FWHM combined with a favourable emission maximum around 880–900 nm. An important condition is however that the luminescence quenching temperature must remain high, preferable above 100 °C. For sensing applications, the intensity is not as high as in high power w-LEDs for lighting where phosphor temperatures can reach 150 °C. Still, thermal quenching can be an issue and in the next section the role of (Si, Ge) mixing on the thermal quenching behaviour is investigated.

3.3. Temperature dependence

To investigate the thermal quenching of the NIR luminescence first the emission intensity was measured as a function of temperature for Cr^{3+} in $LiScSi_2O_6$ and $NaScSi_2O_6$ under 460 nm excitation. The results are shown in Fig. 7. The intensity starts to diminish above ~125 °C with a T_{50} (temperature at which the intensity drops to 50% of the maximum) around 250 °C, consistent with previous studies [10,22]. This high T_{50} for long wavelength Cr^{3+} emission (maximum between 850 and 900 nm) is favourable for application. Typically, high quenching temperatures for broad band $^4T_2$ emission are observed for shorter wavelength Cr^{3+} emission while longer wavelength NIR emission has lower T_{50} values. The high T_{50} combined with redshifted emission make Cr^{3+}-doped $LiScSi_2O_6$ and $NaScSi_2O_6$ promising for application in NIR-LEDs.

Measuring emission intensity as function of temperature to probe thermal quenching can give deviations, for example when the oscillator strength of the absorption transition is temperature dependent giving rise to intensity variations not related to thermal quenching [36,37]. In addition to fundamental problems also trivial aspects such as changes in alignment, collection efficiency or excitation source intensity can give rise to intensity variations not related to thermal quenching. A fast and reliable method to determine T_{50} is measuring the emission lifetime as a function of temperature. As non-radiative decay sets in, the emission lifetime shortens. Temperature dependent lifetime measurements were done on all compounds between −190 and 450 °C. In the SI (Fig. S3 and S4) lifetime measurements are shown with the fits from which the (average) lifetime was determined. In Fig. 8 the temperature dependence of the Cr^{3+} emission life times is plotted for both $NaSc(Si_{1-x}Ge_x)_2O_6$ and $LiSc(Si_{1-x}Ge_x)_2O_6$.

For the $NaSc(Si_{1-x}Ge_x)_2O_6$ series we observe that emission lifetimes are constant up to a certain temperature above which τ rapidly drops. From the temperature dependence the T_{50} values were determined and plotted as a function of Ge content in Fig. 6c. It is evident that increasing the Ge-content lowers the T_{50} values. To fit the temperature dependence

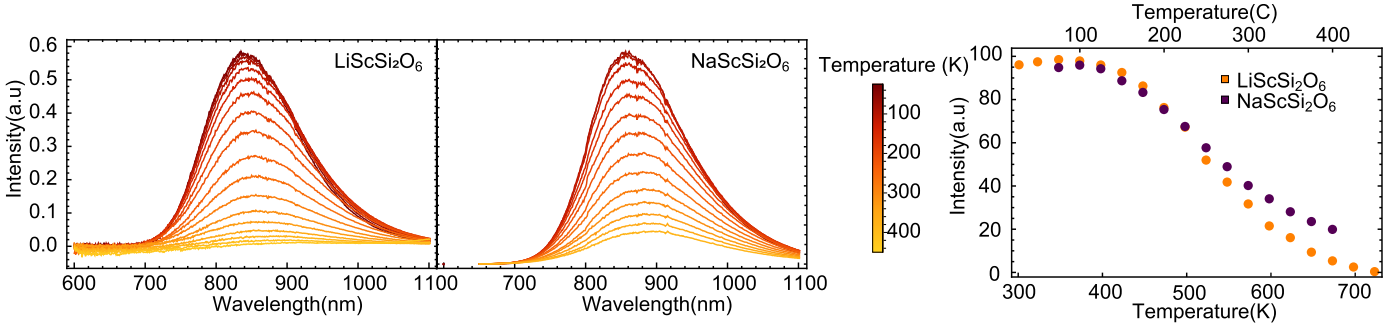

Fig. 7. Temperature dependent emission spectra of LiScSi2O6 and Na ScSi2O6 doped with 3.5% Cr3+ for 460 nm excitation. On the right hand side, the integrated emission intensity is shown as a function of temperature.

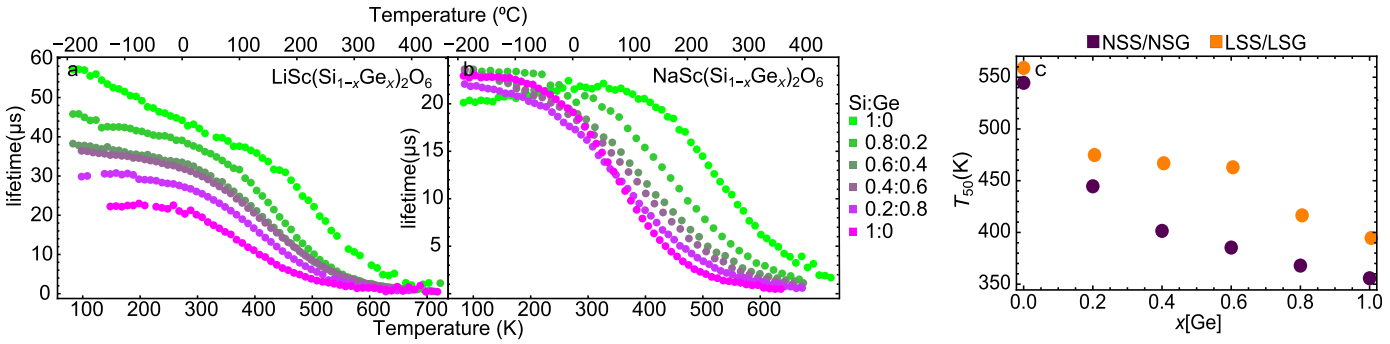

Fig. 8. Average lifetime of $LiSc(Si_{1-x}Ge_x)_2O_6$:1%Cr^{3+}(left) and $NaSc(Si_{1-x}Ge_x)_2O_6$:1%Cr^{3+} (middle) as a function of temperature. From green to purple we go from Silica rich samples to Germanate rich samples. Note the difference in scale on y axis. On the right the T_{50} values are shown as a function of Ge content.

of emission life times, a sigmoidal fit was done [38]:

$$\tau(T) = \frac{\tau(0)}{1 + Ae^{-\Delta E/kT}} \quad (3)$$

Here τ *(0)* is the lifetime a 0 K, assumed to be equal to the lifetime measured at ~80–100 K, *A* is a pre-factor often associated with an attempt rate and *ΔE* is the activation barrier for non-radiative decay to the ground state. A single sigmoidal fit was unsatisfactory for the solid solutions. It can be argued that a multi sigmoidal fit is necessary because the local environment of Cr^{3+} varies from ion to ion in the mixed (Si,Ge) samples. A two sigmoidal fit turned out to be sufficient and was used to determine the T_{50} by using $\tau(T_{50}) = 0.5*\tau(0)$ as shown in Fig. 8. The T_{50} decreases from 539 K to 356 K upon replacing Si by Ge.

For the LSS/LSG series the temperature dependence of the emission lifetime shows a slow decrease prior to the fast drop around 400 K. This is interesting as the intensity does not drop until 450 K (see Fig. 7). This increase in lifetime upon cooling to cryogenic temperatures is also observed for Cr^{3+} emission in solid solutions, albeit less pronounced as the Ge content increases. Similar observations have been made for Cr^{3+} emission in other high symmetry crystals with long emission lifetimes at low temperatures, e.g. in garnets where the lifetime at room temperature is close to 70 μs [39]. A similar behaviour has also been observed for Mn^{4+} where it was shown that thermal occupation of odd parity vibrational modes contribute to relaxing the parity selection rule at elevated temperatures [40]. The temperature dependence follows:

$$\tau_r(T) = \frac{\tau_r(0)}{\coth(h\nu/2kT)} \quad (4)$$

With τ_r *(T)* the radiative lifetime as a function of temperature and $\tau_r(0)$ is the radiative lifetime at 0 K. hν is the effective energy of odd-parity phonon modes and k is the Boltzmann constant. The measured lifetime is determined by the sum of radiative and non-radiative decay rates. Therefore, the equation for to the temperature dependence of the radiative decay time in Eq. (4) needs to be incorporated in the sigmoidal fit Eq. (3):

$$\tau(T) = \frac{\tau_r(T)}{1 + \frac{\tau_r(T)}{\tau_{nr}} e^{-\Delta E/kT}} \quad (5)$$

The decrease in lifetime by phonon coupling at elevated temperatures as is observed for Cr^{3+} in LSS but not in NSS, can be understood from the much stricter parity selection rule in the higher symmetry coordination in LSS. The radiative decay time at 4 K is almost 60 μs in LSS vs. 20 μs in NSS. The static odd-parity crystal field components already relax the selection rule in NSS and the additional contribution from thermally populated odd parity vibrations is not significant. Upon increasing the Ge-content, the low temperature radiative decay rate in the $LiSc(Si_{1-x}Ge_x)_2O_6$ series increases and a single sigmoidal fit can be used to determine the T_{50} for LSG. To model the temperature dependence for LSS/LSG solid solutions taking into account both the disorder in Si/Ge coordination and the temperature dependence of the radiative decay rate gives too many fit parameters. Either equation (5) or a bi-sigmoidal fit gave a reliable fit with similar outcomes for T_{50}. A bi-sigmoidal fit was used for the $LiSc(Si_{0.2}Ge_{0.8})_2O_6$ and Eq. (5) was used for $LiSc(Si_{1-x}Ge_x)_2O_6$ were x = 0,0.2,0.4,0.6. The fits are shown in the SI. Using Eq. (5) LSS gives a vibrational energy hν of 203 cm^{-1}. This is a very reasonable value as low phonon energy phonon in these clinopyroxenes are around 200 cm^{-1} [41] and are typical for Sc–O or Cr–O stretching vibrations. Note that asymmetric stretching or bending vibrations in the $[CrO_6]$ can be expected to distort the inversion symmetry and break the parity selection rule to increase the radiative decay rate. The higher energy stretching vibrations in the SiO_4 or GeO_4 groups will give rise to smaller distortions for Cr^{3+}. The T_{50} values for Cr^{3+} in the LSS/LSG series decrease from 553 K to 393 K changing the Ge content from 0 to 100%.

The variations in quenching temperatures can be understood using the well-known configurational coordinate diagram. Previous research has shown that the dominant temperature quenching mechanism for $^4T_2$ emission from Cr^{3+} is cross-over to the $^4A_2$ ground state by thermal population of higher vibrational levels [6,24,25,42,43]. A larger off-set between ground and excited state parabola lowers the thermal activation energy for this process. Also, a longer wavelength emission (smaller energy difference between ground and excited states) lowers the barrier for non-radiative relaxation. For the Li containing samples the quenching temperatures are higher, both for the germanate and the silicate series. The smaller Li cation creates more rigid crystal structure due to its higher ionic character resulting in a smaller offset between the ground and excited state parabola and thus a higher thermal quenching temperature. Similarly, the more covalent bonding in the germanates vs. the silicates explains the lower T_{50} values with increasing Ge content resulting in a larger offset between ground and excited state, in addition to a redshift of the emission which also contributes to lowering T_{50}.

The optical spectroscopy experiments on Cr^{3+} luminescence in $NaSc(Si_{1-x}Ge_x)_2O_6$ and $LiSc(Si_{1-x}Ge_x)_2O_6$ show that the emission band broadens and redshifts towards 900 nm by partial replacement of Si ion by Ge ions. Both effects are advantageous for application NIR-LEDs where broad band emission between 700 and 1100 nm is desired. However, increasing the Ge-content lowers the thermal quenching temperature which is a drawback for application. Based on the experimental results, an optimum Ge-content is 20–40% which gives rise to an appreciable redshift and broadening while keeping the thermal quenching temperature high enough for application in NIR-LEDs. In addition, a favourable characteristic of the $NaSc(Si_{1-x}Ge_x)_2O_6$ and $LiSc(Si_{1-x}Ge_x)_2O_6$ is the one-dimensional character with small nearest neighbour distances of 3.3 Å for Cr^{3+} in the one direction and nearest neighbour distance of 5.6 Å and 7.7 Å in the other dimension. This gives rise to one-dimensional energy migration and hampers three-dimensional energy migration leading to concentration quenching at high Cr^{3+} concentrations. Incorporating high Cr^{3+} concentrations without quenching is favourable to enhance the absorption strength.

3.4. FTIR/DFT

Infrared active phonons can facilitate parity forbidden d-d transitions such as the $^4T_2$ to $^4A_2$ transition in LSS by temporary inducing odd parity crystal field components. This can explain the temperature induced shortening of the $^4T_2$ to $^4A_2$ emission lifetime in LSS between 100 and 400 K as phonon modes are thermally occupied. To map the energies of phonons in the various host lattices, Fourier Transform Infrared (FTIR) absorption spectroscopy were recorded on undoped NSS/LSS/NSS/NSG. As shown in Fig. 9.

In the IR absorption spectra we observe that the germanates have similar spectra and in parallel the silicates also have similar spectra. The silicates have two groups of peaks, one below 700 cm^{-1} and a second group between 800 and 1200 cm^{-1}. For the germanates both groups are shifted to lower energies, the first group of peaks ending around 600 cm^{-1} and the second group situated between 700 and 900 cm^{-1}. The high energy vibrations are assigned to local modes in the silicate and germanate groups. Si–O stretching vibrations are typically observed around 1000 cm^{-1}. As Si is lighter than Ge the energy required for the vibration is higher. For the Ge–O stretching vibrations are around 800 cm^{-1}. Replacement of Li with Na in both samples causes only minor changes. The replacement of Si with Ge has more influence on the lower energy vibrational modes than replacing Na with Li.

To further investigate the phonon energies, DFT calculations were made on $LiScSi_2O_6$ and $LiScGe_2O_6$. Experimentally determined structures($LiScSi_2O_6$: ICSD #55172 for C2/c, #152075 for $P2_1/c$, $LiScGe_2O_6$: #430516 for $P2_1/c$) are used as initial geometries. For C2/c phase of $LiScGe_2O_6$, the optimized structure of $LiScSi_2O_6$ is used as an initial structure because of no experimental structure data. The atomic structures were fully optimized by minimizing the electronic total energy and Hellmann-Feynman forces [44]. In $LiScSi_2O_6$, no energy difference between C2/2 and $P2_1/c$ structure is observed. However, $P2_1/c$ structure is stable in $LiScGe_2O_6$. This result agrees with experimental observations. After the structural optimization of the unit cell the phonon dispersion was calculated for both hosts.

In Fig. 10 the phonon energies at the Γ point are overlaid with the FTIR of the respective compound. There is good agreement between the experimentally observed and calculated vibrational energies. The gap in vibrational states between 700 and 800 cm^{-1} for LSS and between 600 and 700 cm^{-1} for LSG agrees with the calculations. The calculated phonon energies extend to 1050 cm-1 for the silicate and to 850 cm-1 for the germanate, again in line with the experimental results. The absorption tail above the highest energy phonons is attributed to multi phonon absorption (combination bands).

It is also interesting to investigate if the observed temperature dependence of the $^4T_2$-$^4A_2$ emission lifetime for Cr^{3+} in $LiScSi_2O_6$ is consistent with energies for odd-parity local modes. The temperature dependence was modelled using equation (4) and the fit gave a phonon energy hν of 202 cm^{-1} (see SI for the fit). The various low energy vibrations were inspected by monitoring the displacements of the atoms, via the xyz jmol files (see SI for the files for LSS/LSG). The 8th lowest phonons clearly create a strong asymmetry on the Sc site, the calculated energy of this vibration is 167 cm^{-1}. The next vibration that distorts the centre of inversion symmetry around Sc significantly are 13 and 14th vibrations, the calculated energies of these vibrations are cm^{-1} 234 and 238 cm^{-1}, respectively. The higher energy levels will have less importance as the phonon population decreases exponentially with increasing energy. As these values correspond well with the effective phonon energy of the fit 202 cm^{-1} this serves as evidence that asymmetric vibrations involving the Cr^{3+} ion and surrounding ligands are responsible for the shortening of the lifetime with increasing temperature for Cr^{3+} in the highest symmetry coordination in LSS.

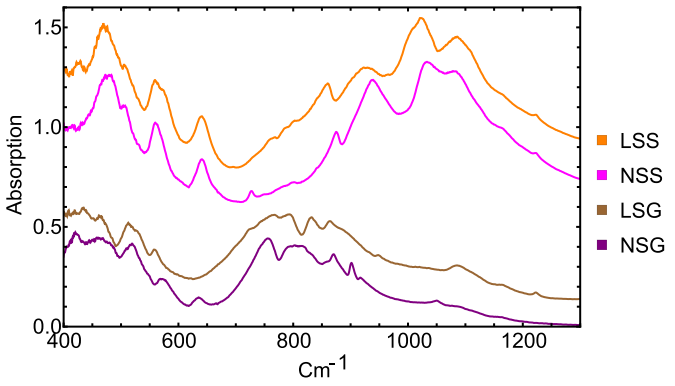

Fig. 9. FTIR measurements on the four undoped host lattices LSS, NSS, LSG and NSG. The vertical offset was introduced for easy comparison.

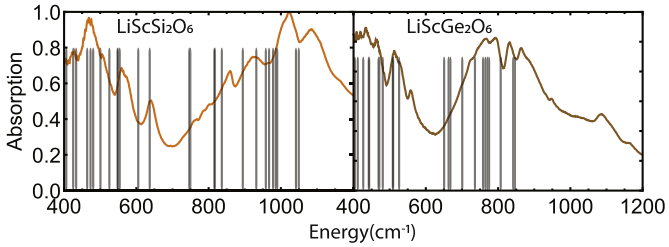

Fig. 10. FTIR absorption measurements of LSS and LSG. The black lines indicate the phonon energies determined using DFT calculations.

4. Conclusion

Better blue excitable phosphors with broad band NIR emission are needed for compact light sources in new NIR sensing applications. Both $LiSc(Si_{1-x}Ge_x)_2O_6$ and $NaSc(Si_{1-x}Ge_x)_2O_6$ doped with Cr^{3+} are promising materials with efficient broad band NIR emission and high luminescence quenching temperatures. The role of partial replacement of Si by Ge on the $^4T_2$-$^4A_2$ emission has been investigated aimed at tuning the NIR emission to longer wavelengths and broadening the NIR emission output. Disorder in the second coordination sphere for mixed Si–Ge compositions broadens the NIR emission band to almost 200 nm. Addition of Ge however also lowers the luminescence quenching temperature. The trends in thermal quenching behaviour can be understood by thermally activated cross-over from the $^4T_2$ excited state to the $^4A_2$ ground state. The optimum spectral properties for application in NIR LEDs are found for in $LiSc(Si_{1-x}Ge_x)_2O_6$:Cr^{3+} with 20–40% of Ge having broad band (FWHM ~180 nm) emission around 900 nm with a thermal quenching temperatures well above 100 °C. In addition, the role of symmetry in the temperature dependence of ratio of $^4T_1/^4T_2$ absorption bands has been discussed indicating the ratio increases for lower symmetry coordination.

Author agreement statement

We the undersigned declare that this manuscript is original, has not been published before and is not currently being considered for publication elsewhere.

We confirm that the manuscript has been read and approved by all named authors and that there are no other persons who satisfied the criteria for authorship but are not listed. We further confirm that the order of authors listed in the manuscript has been approved by all of us.

We understand that the Corresponding Author is the sole contact for the Editorial process. He/she is responsible for communicating with the other authors about progress, submissions of revisions and final approval of proofs.

Signed by all authors as follows:

CRediT authorship contribution statement

Arnoldus J. van Bunningen: Writing – original draft, Formal analysis, Investigation, Resources, Data curation. **Atul D. Sontakke:** Investigation, Resources. **Sadakazu Wakui:** Formal analysis. **Andries Meijerink:** Conceptualization, Writing – review & editing.

Declaration of competing interest

The authors declare the following financial interests/personal relationships which may be considered as potential competing interests:

Arnoldus J. van Bunningen, Atul D. Sontakke, Andries Meijerink have patent Light emitting device (European patent application No. 21172494.3) pending to NICHIA CORPORATION and Universiteit Utrecht Holding B.V.

Acknowledgement

The authors want to thank Nichia Corporation for their generous contribution funding this research.

Appendix A. Supplementary data

Supplementary data to this article can be found online at https://doi.org/10.1016/j.optmat.2022.112433.

References

[1] P.M. Pattison, J.Y. Tsao, G.C. Brainard, B. Bugbee, LEDs for photons, physiology and food, Nature 563 (7732) (22-Nov-2018) 493–500. Nature Publishing Group.
[2] J. Lai, et al., Broadband near-infrared emitting from Li1.6Zn1.6Sn2.8O8:Cr3+ phosphor by two-site occupation and Al3+ cationic regulation, Mater. Des. 192 (Jul. 2020), 108701.
[3] An Introduction to Near Infrared (NIR) Spectroscopy, IM Publications Open, [Online]. Available: https://www.impopen.com/introduction-near-infrared-nir-spectroscopy. (Accessed 8 March 2021).
[4] [Online]. Available: OSLON® P1616, SFH 4737 https://www.osram.com/ecat/OSLONP1616SFH4737/com/en/class_pim_web_catalog_103489/prd_pim_device_10751075/.
[5] B. Malysa, A. Meijerink, T. Jüstel, Temperature dependent Cr3+ photoluminescence in garnets of the type X3Sc2Ga3O12 (X = Lu, Y, Gd, La), J. Lumin. 202 (February) (Oct. 2018) 523–531.
[6] L. Zhang, et al., Cr 3+ -doped broadband NIR garnet phosphor with enhanced luminescence and its application in NIR spectroscopy, Adv. Opt. Mater. 7 (12) (Jun. 2019), 1900185.
[7] S. Miao, et al., Spectrally tunable and thermally stable near-infrared luminescence in Na 3 Sc 2 (PO 4) 3 :Cr 3+ phosphors by Ga 3+ co-doping for light-emitting diodes, J. Mater. Chem. C 10 (3) (Jan. 2022) 994–1002.
[8] D. Huang, et al., A highly efficient and thermally stable broadband Cr3+-activated double borate phosphor for near-infrared light-emitting diodes, J. Mater. Chem. C 9 (1) (Jan. 2021) 164–172.
[9] S. Kück, L. Fornasiero, E. Mix, G. Huber, Spectroscopic properties of Cr-doped Sc2O3, J. Lumin. 87 (89) (May 2000) 1122–1125.
[10] Q.I.S. Hao, et al., Broadband near-infrared light source derived from Cr 3+ -doped phosphors and a blue LED chip, Opt. Lett. 43 (21) (Nov. 2018) 5251.
[11] Y. Duan, Y. Liu, G. Zhang, L. Yao, Q. Shao, Broadband Cr3+-sensitized upconversion luminescence of LiScSi2O6:Cr3+/Er3+, J. Rare Earths 39 (10) (Oct. 2021) 1181–1186.
[12] M. Bockstedte, A. Kley, J. Neugebauer, M. Scheffler, Density-functional theory calculations for poly-atomic systems: electronic structure, static and elastic properties and ab initio molecular dynamics, Comput. Phys. Commun. 107 (1–3) (Dec. 1997) 187–222.
[13] P. Hohenberg, W. Kohn, Inhomogeneous electron gas, Phys. Rev. 136 (3B) (Nov. 1964) B864.
[14] W. Kohn, L.J. Sham, Self-consistent equations including exchange and correlation effects, Phys. Rev. 140 (4A) (Nov. 1965) A1133.
[15] G. Kresse, J. Furthmüller, Efficient iterative schemes for *ab initio* total-energy calculations using a plane-wave basis set, Phys. Rev. B 54 (16) (Oct. 1996) 11169.
[16] G. Kresse, D. Joubert, From ultrasoft pseudopotentials to the projector augmented-wave method, Phys. Rev. B 59 (3) (Jan. 1999) 1758.
[17] J.P. Perdew, K. Burke, M. Ernzerhof, Generalized gradient approximation made simple, Phys. Rev. Lett. 77 (18) (Oct. 1996) 3865.
[18] S. Baroni, P. Giannozzi, A. Testa, Green's-function approach to linear response in solids, Phys. Rev. Lett. 58 (18) (May 1987) 1861.
[19] X. Gonze, Perturbation expansion of variational principles at arbitrary order, Phys. Rev. 52 (2) (Aug. 1995) 1086.
[20] A. Togo, I. Tanaka, First principles phonon calculations in materials science, Scripta Mater. 108 (Nov. 2015) 1–5.
[21] R.D. Shannon, Revised Effective Ionic Radii and Systematic Studies of Interatomie Distances in Halides and Chaleogenides, 1976.
[22] Y. Yan, et al., Photoluminescence properties of AScSi2O6:Cr3+(A = Na and Li) phosphors with high efficiency and thermal stability for near-infrared phosphor-converted light-emitting diode light sources, ACS Appl. Mater. Interfaces 14 (Feb) (2021).
[23] U. Fano, Effects of configuration interaction on intensities and phase shifts, Phys. Rev. 124 (6) (Dec. 1961) 1866–1878.
[24] S. Adachi, Luminescence spectroscopy of Cr3+ in an oxide: a strong or weak crystal-field phosphor? J. Lumin. 234 (Feb. 2021), 117965.
[25] S. Miao, Y. Liang, Y. Zhang, D. Chen, X.J. Wang, Broadband short-wave infrared light-emitting diodes based on Cr3+-doped LiScGeO4Phosphor, ACS Appl. Mater. Interfaces 13 (30) (Aug. 2021) 36011–36019.
[26] Z. Jia, et al., Strategies to approach high performance in Cr3+-doped phosphors for high-power NIR-LED light sources, Light Sci. Appl. 9 (1) (Dec. 2020) 86.
[27] J. Mooney, P. Kambhampati, Get the basics right: jacobian conversion of wavelength and energy scales for quantitative analysis of emission spectra, J. Phys. Chem. Lett. 4 (19) (Oct. 2013) 3316–3318.
[28] B. Malysa, A. Meijerink, W. Wu, T. Jüstel, On the influence of calcium substitution to the optical properties of Cr3+ doped SrSc2O4, J. Lumin. 190 (April) (Oct. 2017) 234–241.
[29] Y. Tanabe, S. Sugano, On the absorption spectra of complex ions II, J. Phys. Soc. Jpn. 9 (5) (Sep. 1954).
[30] G. Wang, H.G. Gallagher, T.P.J. Han, B. Henderson, The growth and optical assessment of Cr3+-doped RX(BO3)4 crystals with R = Y, Gd; X = Al, Sc, J. Cryst. Growth 163 (3) (Jun. 1996) 272–278.
[31] Z. Nie, et al., Spectroscopic investigation of CaAl12O19:M 3+ upon UV/vacuum-UV excitation: a comparison with SrAl 12O19:M3+ (M ≤ Pr,Cr), J. Phys. Condens. Matter 19 (7) (Feb. 2007) 76204.
[32] F.C. Hawthorne, H.D. Grundy, The Canadian mineralogist, Mineral. Assoc. Can. 15 (1) (1977).
[33] E.A. Genkina, B.A. Maksimov, V.A. Timofeeva, A.B. Bykov, Crystal structure of sodium scandium germanate NaScGe2O6, J. Struct. Chem. 26 (1) (Jan. 1985) 136–138.
[34] M. Back, et al., Boltzmann thermometry in Cr^{3+} -doped Ga_2O_3 polymorphs: the structure matters!, Adv. Opt. Mater. (Feb. 2021), 2100033.
[35] D. Chen, X. Chen, X. Li, H. Guo, S. Liu, X. Li, Cr^3+-doped Bi_2Ga_4O_9-Bi_2Al_4O_9 solid-solution phosphors: crystal-field modulation and lifetime-based temperature sensing, Opt. Lett. 42 (23) (Dec. 2017) 4950.
[36] T. Senden, R.J.A. Van DIjk-Moes, A. Meijerink, Quenching of the red Mn4+ luminescence in Mn4+-doped fluoride LED phosphors, Light Sci. Appl. 7 (1) (Dec. 2018) 2047–7538.
[37] D. Böhnisch, J. Rosenboom, A. García-Fuente, W. Urland, T. Jüstel, F. Baur, On a blue emitting phosphor $Na_3RbMg_7(PO_4)_6:Eu^{2+}$ showing ultra high thermal stability, J. Mater. Chem. C 7 (20) (May 2019) 6012–6021.
[38] A.M. Srivastava, H.A. Comanzo, S. Camardello, S.B. Chaney, M. Aycibin, U. Happek, Unusual luminescence of octahedrally coordinated divalent europium ion in Cs2M2+P2O7 (M2+=Ca, Sr), J. Lumin. 129 (9) (Sep. 2009) 919–925.
[39] G. Özen, Temperature effect on the radiative and non-radiative processes in LLGG: Cr3+, Nd3+, Opt Commun. 183 (5) (Sep. 2000) 493–501.
[40] T. Senden, E.J. van Harten, A. Meijerink, Synthesis and narrow red luminescence of Cs2HfF6:Mn4+, a new phosphor for warm white LEDs, J. Lumin. 194 (Feb. 2018) 131–138.
[41] P. Vignola, N. Rotiroti, F. Hatert, D. Bersani, S. Andò, S. Varvello, Jervisite, NaScSi2O6: optical data, morphology, Raman spectroscopy, and crystal chemistry, Can. Mineral. 57 (4) (Jul. 2019) 489–498.
[42] J. Xiang, et al., Synthesis of broadband NIR garnet phosphor Ca 4 ZrGe 3 O 12 : Cr 3+ , Yb 3+ for NIR pc-LED applications, Mater. Chem. Front. 6 (4) (Feb. 2022) 440–449.
[43] T. Gao, W. Zhuang, R. Liu, Y. Liu, C. Yan, X. Chen, Design of a broadband NIR phosphor for security-monitoring LEDs: tunable photoluminescence properties and enhanced thermal stability, Cryst. Growth Des. 20 (6) (Jun. 2020) 3851–3860.
[44] R.P. Feynman, Forces in molecules, Phys. Rev. 56 (4) (Aug. 1939) 340–343.
[45] G.J. Redhammer, G. Roth, Structural changes upon the temperature dependent C2/c → P21/c phase transition in LiMe3+Si2O6 clinopyroxenes, Me = Cr, Ga, Fe, V, Sc and in, Z. für Kristallogr. - Cryst. Mater. 219 (10) (Jan. 2004) 585–605.
[46] G. Hofer, J. Kuzel, K.S. Scheidl, G. Redhammer, R. Miletich, High-pressure crystallography and compression behavior of the alkali-scandium-germanate end-members LiScGe2O6 and NaScGe2O6, J. Solid State Chem. 229 (Jun. 2015) 188–196.